Check for updates

Vorticity and divergence at scales down to 200 km within and around the polar cyclones of Jupiter

Andrew P. Ingersoll [1]✉, Shawn P. Ewald[1], Federico Tosi[2], Alberto Adriani[2], Alessandro Mura[2], Davide Grassi[2], Christina Plainaki[3], Giuseppe Sindoni[3], Cheng Li[4], Lia Siegelman [5], Patrice Klein [6,7,8] and William R. Young[5]

Since 2017 the Juno spacecraft has observed a cyclone at the north pole of Jupiter surrounded by eight smaller cyclones arranged in a polygonal pattern. It is not clear why this configuration is so stable or how it is maintained. Here we use a time series of images obtained by the JIRAM mapping spectrometer on Juno to track the winds and measure the vorticity and horizontal divergence within and around the polar cyclone and two of the circumpolar ones. We find an anticyclonic ring between the polar cyclone and the surrounding cyclones, supporting the theory that such shielding is needed for the stability of the polygonal pattern. However, even at the smallest spatial scale (180 km) we do not find the expected signature of convection—a spatial correlation between divergence and anticyclonic vorticity—in contrast with a previous study using additional assumptions about the dynamics, which shows the correlation at scales from 20 to 200 km. We suggest that a smaller size, relative to atmospheric thickness, of Jupiter's convective storms compared with Earth's, can reconcile the two studies.

At Jupiter's north pole there are eight cyclones that form an octagon, with one cyclone at each vertex and one additional cyclone in the centre[1,2]. The centres of the cyclones are at latitudes of $83 \pm 10°$, which is about 8,700 km from the pole. Jupiter's south pole is the same, except there are only five cyclones, which form a pentagon with one at the centre. The vertices are at latitudes of $-83 \pm 1°$. The polygons and the individual vortices that comprise them have been stable for the 4 years since Juno discovered them[3–5]. The polygonal patterns rotate slowly, or not at all. The peak azimuthal wind speeds around each vortex range from 70 to $100 \, \mathrm{m \, s^{-1}}$, and the radial distance r from the peak to the vortex centre is about 1,000 km (ref. [6]). In contrast, Saturn has only one vortex, a cyclone, at each pole[7]. The peak winds are $150 \, \mathrm{m \, s^{-1}}$, and the radius at the peak is 1,500 km (refs. [8,9]). Saturn has a six-lobed meandering jet at 75°, but it has no cyclones associated with it. Both laboratory and theoretical models treat the hexagon as a stable wave-like pattern[10–14].

There have been a handful of theoretical studies that specifically address the origin of polar cyclones on Jupiter and Saturn[15–18]. They comprise one- and two-layer models that introduce small-scale motions either as an initial condition or as continuous forcing balanced by dissipation. The small-scale vortices merge and become the large-scale vortices. The cyclones drift polewards, and the anticyclones drift equatorwards, as they do on Earth. In some cases the cyclones merge into one big cyclone at the pole. In other cases, with different parameter settings, the cyclones wander about without forming polygons. Only one theoretical study obtained stable polygons from random initial conditions, and only when the wavelengths of the initial random disturbances are less than 300 km (ref. [19]). A Fourier analysis of Juno data reveals that flows with wavelengths larger than 215 km are gaining energy from smaller-scale flows—an example of an upscale energy transfer[20]. Therefore, one

goal of this Article is to measure vorticity and divergence at scales much smaller than the main cyclones and determine how the upscale energy transfer takes place.

Another theoretical study[21], which used shallow water equations, introduced cyclones that have the observed gross properties—maximum velocity and radius—and arranged them into different polygonal patterns around the pole to see which ones are stable. The stable ones have shielding (a ring of anticyclonic vorticity surrounding each of the cyclones) and the unstable ones do not. Some models with small-scale forcing develop shielding, but they do not organize into polygons[15–18,22]. So another goal of this Article is to measure the vorticity inside and outside the large cyclones and see whether they are shielded.

The small-scale forcing in the one- and two-layer models is a crude representation of convection. There are 3D models that treat convection explicitly, in some cases with the Boussinesq (quasi-incompressible) approximation[23–25] and in other cases with density varying vertically by up to five scale heights[25–28]. Some treat fluid in a box with periodic boundary conditions, and others use full spherical geometry. All the 3D models have small-scale convective plumes. The convective plumes produce large-scale vortices by mergers, an upscale transfer of kinetic energy, and some of the vortices arrange themselves into polygonal patterns[23,28]. Although a relation between divergence and vorticity is not discussed in any of these models, a negative correlation is expected for convection on a rotating planet. Therefore, a third goal of this Article is to measure divergence and vorticity at scales down to 180 km and search for this signature of convection.

Results

Scale analysis. At mid-latitudes one important parameter is the length, $L_\beta = (U/\beta)^{1/2}$, where U is a characteristic horizontal

[1]Planetary Science, California Institute of Technology, Pasadena, CA, USA. [2]Istituto Nazionale di AstroFisica – Istituto di Astrofisica e Planetologia Spaziali (INAF-IAPS), Rome, Italy. [3]Agenzia Spaziale Italiana (ASI), Rome, Italy. [4]Climate and Space Sciences and Engineering, University of Michigan, Ann Arbor, MI, USA. [5]Scripps Institution of Oceanography, University of California, San Diego, La Jolla, CA, USA. [6]Division of Geological and Planetary Sciences, California Institute of Technology, Pasadena, CA, USA. [7]Jet Propulsion Laboratory, California Institute of Technology, Pasadena, CA, USA. [8]LMD/IPSL, Ecole Normale Supérieure, CNRS, Paris, France. ✉e-mail: api@gps.caltech.edu

velocity and $\beta = df/dy = 2\Omega\sin\theta/a$ is the latitudinal gradient of the planetary vorticity $f = 2\Omega\cos\theta$. Here θ is colatitude, y is the northward coordinate, and a and Ω are the planet's radius and angular velocity, respectively. L_β plays a role in the stability of the zonal jets. On both Jupiter and Saturn, $2\pi/L_\beta$ is approximately equal to the wavenumber of the zonal jet profile with respect to latitude when U is the root mean squared speed[29–33]. However, L_β is infinite at the poles as β linearly approaches zero there. We therefore introduce a different scaling[19], one based on the inverse gradient of β at the pole, $\gamma = -d\beta/dy = 2\Omega/a^2$. The associated length scale is $L_\gamma = (U/\gamma)^{1/3}$, and for $U = 80\,\mathrm{m\,s^{-1}}$ it is about 10,500 km (we ignore the oblateness and use Jupiter's equatorial radius throughout this paper). L_γ represents the radius of the circle around the pole inside which the effect of the vortices—large-scale turbulence—is greater than the effect of β and the zonal jets. Note that L_γ is the distance from a specific point (the pole) and L_β is not. The value of L_γ is close to the 8,700 km size of the polygons on Jupiter.

The radius of deformation L_d is c/f, where c is the gravity wave speed of the gravest vertical mode—the one spanning Jupiter's weather layer, which extends from the base of the stratosphere down to the base of the water cloud. The value of c depends on the degree of stratification of the weather layer[34], and is assumed to be independent of latitude. Different assumptions about the vertical stratification put the average L_d at the poles in the range 350–1,300 km (refs. [34–36]). This brackets the 1,000 km radius of the cyclones.

Originally L_β was defined as the length scale where the flow transitions from turbulence to zonal jets as the scale of the flow increases[37]. Observations of Jupiter suggest that a similar transition occurs as the latitude of the flow decreases. The critical latitude, below which zonal jets dominate, was shown to be a decreasing function of L_d (refs. [38,39]). Here we argue that a critical latitude, $\pi/2 - L_\gamma/a$, exists even for arbitrarily small values of L_d.

We discuss the observations using parameters of the shallow water equations, where a single layer of fluid of thickness h floats hydrostatically on a much thicker fluid, which we assume is at rest[40,41]. The two dependent variables are the horizontal velocity $\mathbf{v}$ and the gravitational potential $\phi = g_r h$, where g_r is the reduced gravity (the gravitational acceleration times the fractional density difference $\Delta\rho/\rho$ between the two layers[41]). Here ϕ is the column density in the 2D continuity equation and $\sqrt{\phi}$ is the gravity wave speed c; ϕ controls vortex stretching and enters in the expression for potential vorticity (PV), which is a dynamical scalar that is conserved in fluid elements. For the shallow water equations PV is $(\zeta + f)/\phi$, where $\zeta = (\nabla \times \mathbf{v}) \cdot \widehat{\mathbf{k}}$ is the relative vorticity (the curl of the horizontal velocity). Three-dimensional effects are not completely ignored: they enter through L_d, which is proportional to the square root of h and the fractional density difference $\Delta\rho/\rho$. Even these quantities are uncertain, so given the paucity of information about vertical structure, it is best to discuss our observations with the shallow water equations.

Vorticity and divergence. Figure 1 shows the octagon of cyclones surrounding the north pole[2]. Features in the clouds are visible at scales down to ~100 km, which is much smaller than the 1,000 km radius where the azimuthal velocity is greatest. The figure was made from infrared images taken by the Jupiter Infrared Auroral Mapper (JIRAM) on 2 February 2017. The JIRAM M filter tracks the clouds at 4.5–5.0 µm wavelengths[42]. The image numbers used in this analysis are listed in Supplementary Table 1. The geometrically located images, projected onto the tangent plane at the pole, are available in Supplementary Data 1. The derived velocity vectors are provided in Supplementary Data 2.

Figure 2 shows vorticity and divergence maps for two independent determinations of the wind field. The measurement required clouds in a pair of JIRAM images separated in time to be tracked to obtain the velocity, and then closed line integrals were taken to get
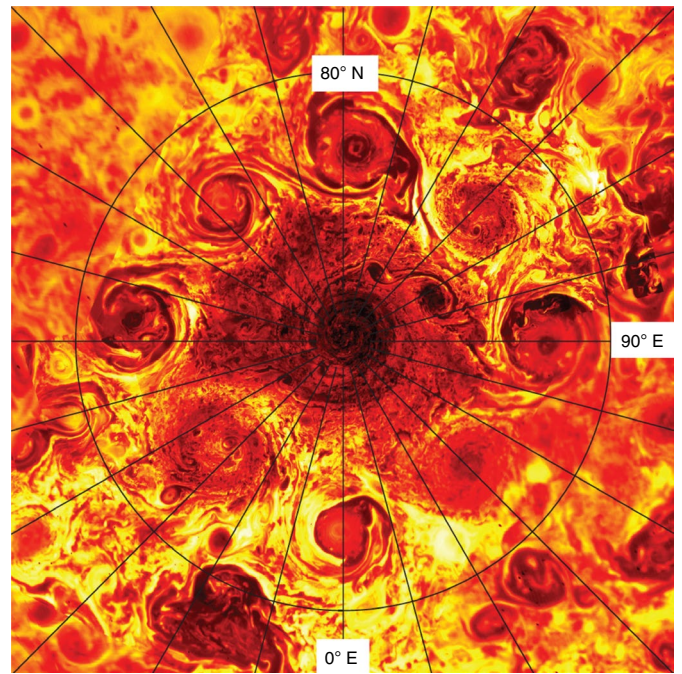

Fig. 1 | Infrared image of the northern hemisphere as seen by JIRAM. The circle at 80° latitude is about 12,000 km from the pole. The lines of constant longitude are 15° apart. The radiances have been corrected for nadir viewing, with bright yellow signifying greater radiance and dark red signifying lesser radiance. The average brightness temperature is in the range 215–220 K. Fig. 2 covers the central cyclone and the two cyclones at 135° and 315° east longitude, respectively. The two dark features at 120–150° E, 86° N whose filaments spiral towards their centres in a clockwise direction are anticyclones. Figure reproduced with permission from ref. [2], Springer Nature Limited.

vorticity and divergence. The magnitude of the vorticity is larger than that of the divergence. The persistence and movement of vorticity features, even those ~180 km in size, shows that the small-scale features are not measurement noise. The motion is visible when one toggles between the left and right vorticity maps in Fig. 2, as can be done with Supplementary Figs. 1–4.

Planetary signal and measurement noise. In Fig. 3, the top two panels show covariances between n0103 and n0204, which are the two independent determinations of the wind fields in Fig. 2. Vorticity is top left, and divergence is top right. If the two measurements gave exactly the same values at each point, the arrays of points would lie on a straight line running from the lower left corner to the upper right corner. Deviations from this line, that is, a correlation coefficient less than 1.0, come partly from measurement noise and partly from cloud motions on the planet. The vorticity measurements have a correlation coefficient η of 0.729. As the measurement noise is uncorrelated with cloud motions on the planet, the noise and planetary variances add up (equation (1)). And given that the noise from n0103 is uncorrelated with that from n0204, the covariations do not contain the variance of measurement noise (equation (2)):

$$\overline{(x-\bar{x})^2} = \overline{(y-\bar{y})^2} = \sigma_P^2 + \sigma_n^2, \overline{(x-\bar{x})(y-\bar{y})} = \sigma_P^2 \qquad (1)$$

$$\frac{\overline{(x-\bar{x})(y-\bar{y})}}{\overline{(x-\bar{x})^2}^{1/2}\,\overline{(y-\bar{y})^2}^{1/2}} = \eta = \frac{\sigma_P^2}{\sigma_P^2 + \sigma_n^2} \qquad (2)$$
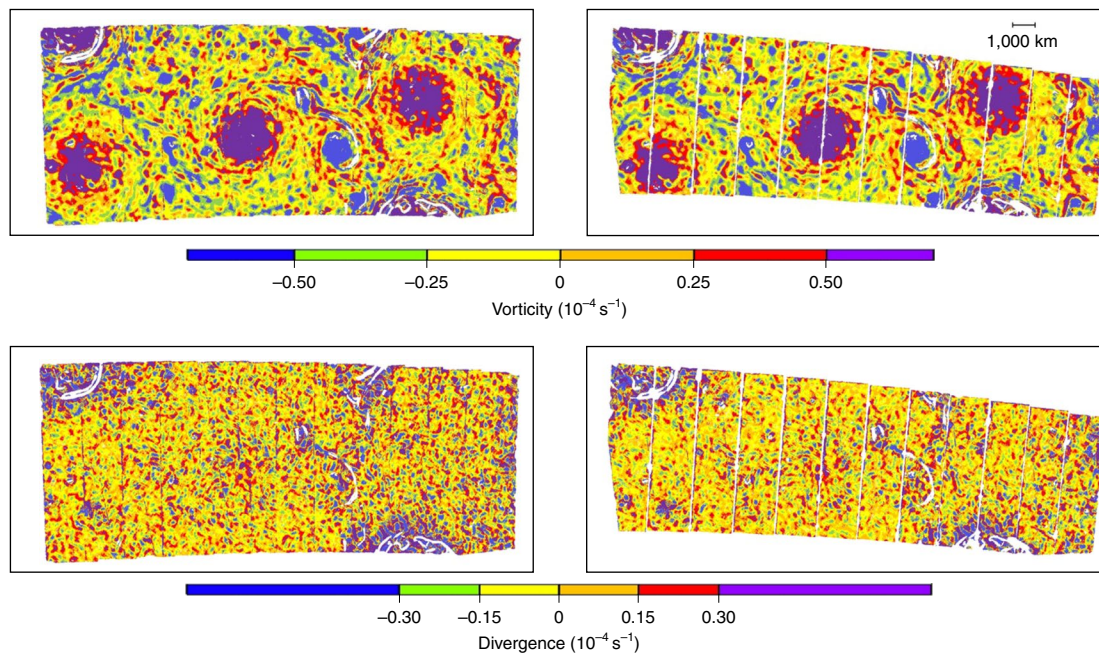
Fig. 2 | Vorticity and divergence derived from two independent determinations of the wind. Top: vorticity. Bottom: divergence. Each determination is derived from two sets of 12 adjacent images, and the sets are ordered in time. n0103 (left) is derived from the first and third sets, which are 16 min apart and overlap in time with the second and fourth sets (n0204, right), which are also 16 min apart. Thus, the interval between n0103 and n0204 is 8 min. The gaps between the 12 images are visible as faint vertical lines, which are especially prominent in n0204. The amorphous white spaces are regions (masks) where the image entropy[51] was below a threshold needed for reliable cloud-tracked wind analysis. They cover 1.8% and 2.1% of the pixels in the left and right determinations, respectively. The entropy histogram, with the dividing line below which the masks were applied, and the images with and without masks, are provided in Supplementary Figs. 5–7. The long dimension of the four large rectangles is ~20,000 km, and the smallest resolved features are ~100 km in diameter. The central cyclone and the two cyclones at lower left and upper right almost disappear in the divergence maps, but the cyclones at upper left and lower right do not, mainly because the image entropy is low and the velocity error is high. The latter two cyclones are at 90° and 270°E in Fig. 1. The resolution of the original images ranges from 22 to 14 km per pixel. The resolution of the derived velocity field is 45 km. We used Gauss' law and Stokes' theorem to calculate divergence and vorticity, integrating around a square box that is 180 km on a side.

The quantities involving x and y are measurements and are known, so the measured correlation coefficient η allows one to separately determine the variance σ_p^2 of vorticity on the planet and the variance σ_n^2 of measurement noise. The same reasoning applies to the divergence (top right panel in Fig. 3).

Table 1 shows the results for different values of the dimensions of the box used to measure vorticity and divergence. For the upper right panel of Fig. 3 and the 180 km × 180 km box, $\eta = 0.299018$, meaning that there is some divergence on the planet, but its variance is less than the measurement noise. Note that the noise values for vorticity and divergence are about the same for the same box size. The difference is that divergence decreases by a factor of 4.34, and vorticity decreases only by a factor of 1.61 from the 90 km × 90 km box to the 360 km × 360 km box. This difference is an indication that the divergence is a small-scale phenomenon that averages out for the larger box sizes. For the lower two panels of Fig. 3, divergence is plotted on the y axis with vorticity on the x axis, and η is essentially zero. Supplementary Table 2 shows that the noise estimates in Table 1 are best fitted by assuming that the measurement uncertainty for each component of velocity is 7.8 m s^{-1}.

Potential vorticity and shielding. Figure 4 shows the azimuthal mean $\bar{v}$ of the azimuthal velocity around the central cyclone as a function of radius r out to 6,000 km. Also shown are the mean relative vorticity $\bar{\zeta}$, the mean gravitational potential $\bar{\phi}$ and the mean potential vorticity $\overline{PV}$. In each panel there are three smooth curves. The middle one, coloured orange, was derived by a linear least squares fit to the velocity data. The basis functions are given in the Methods. The profile of $\bar{v}(r)$ agrees with earlier estimates[6],

including the profile at $r > 2,000$ km falling off faster than $1/r$, implying negative vorticity in that region. Note that the fitted curve fits the data even where the velocity becomes negative (clockwise) at 4,000–6,000 km radial distance. The tabulated data are in Supplementary Data 3.

Bottom left: the ϕ values in Fig. 4 were computed from an integral and are therefore uncertain by an additive constant. However, $\phi = g_r h$ is proportional to the thickness, and the thickness cannot be negative. The local maximum of ϕ is at $r = 4,075$ km, and Fig. 4 was computed with $\phi = 124 \times 10^3$ m^2 s^2 there. Having $\phi > 0$ at the origin requires $\phi > 69 \times 10^3$ m^2 s^2 at $r = 4,075$ km. This gave $L_d > \sqrt{\bar{\phi}}/f = 749$ km at $r = 4,075$ km, which is in the middle of the estimates obtained from lower latitudes when the variation in f with latitude was taken into account[34–36].

Discussion

In a shallow water model that starts with cyclones of the observed size and velocity arrayed in polygonal patterns around the Jovian pole, stability requires an anticyclonic ring (shielding) around each cyclone[21]. With a peak azimuthal velocity of 80 m s^{-1} and radius at the peak of 1,000 km, a single parameter (b) controls the shape of the velocity profile and the depth of the shielding. The other free parameter is L_d, but it has only a small effect on the results. The polygons are mainly stable in the range $1 < b < 2$. Below this range, the shielding is too weak and the vortices merge. Above this range, the negative vorticity is too strong and the anticyclonic rings become two satellites orbiting around the cyclone 180° apart. At $b > 3$, these tripoles are unstable and the polygons fly apart chaotically. The blue curve in Fig. 4 has $b = 1.35$, which is safely in the stable zone
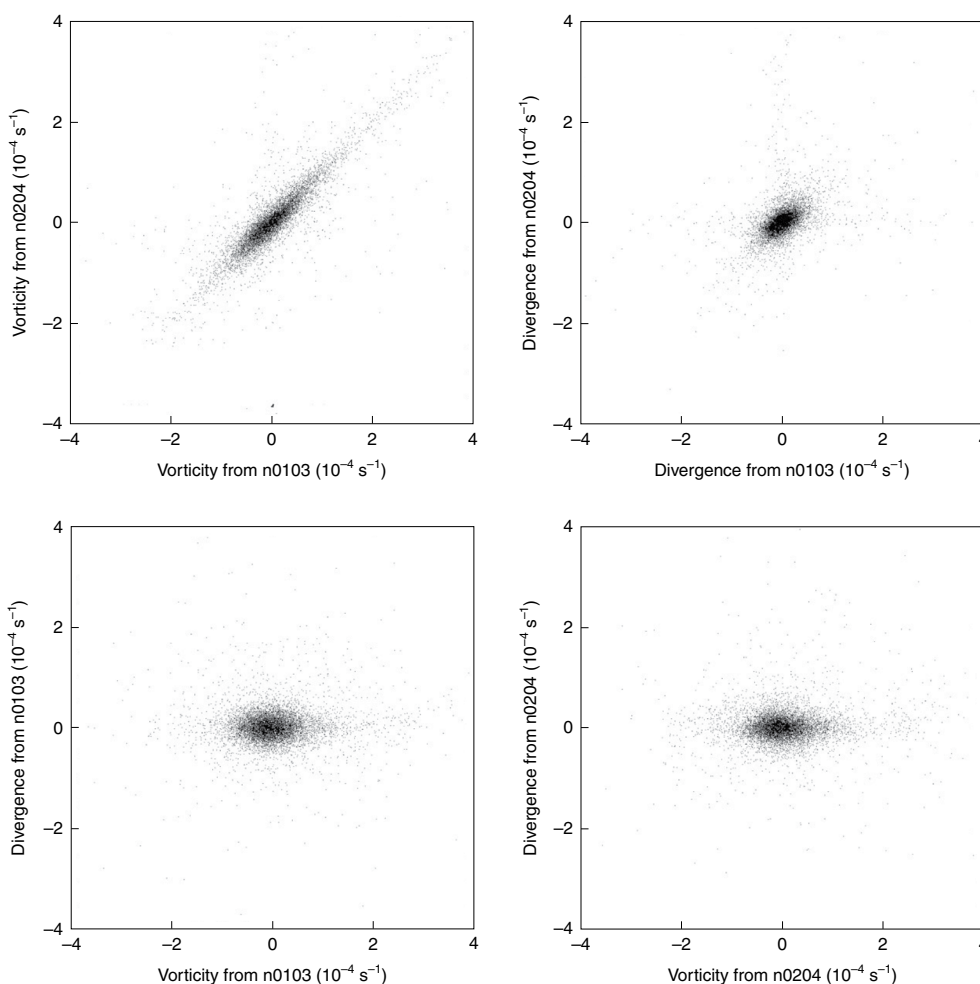
Fig. 3 | Covariances of the vorticity and divergence fields. Each point on the graphs comes from a unique point on the planet as determined both from n0103 and from n0204 (Fig. 2). Top: vorticity (left) and divergence (right) are plotted from the two independent determinations at those points, with the n0204 determination on the vertical axis and the n0103 determination on the horizontal axis. The time interval between the two determinations is 8 min. At 80 m s⁻¹, which is about the maximum speed of the clouds, a feature moves 38 km. This is considerably less than the 180 km box size used to measure vorticity and divergence. Thus, to a good approximation, the two determinations show the same cloud features at the same time. The small motion is still visible, however, when it takes place on a large scale and includes many small-scale, high-contrast features, as with the slight rotation of the features visible in Fig. 2 and Supplementary Figs 1–4. Bottom: points are plotted with divergence on the vertical axis and vorticity on the horizontal axis for n0103 (left) and n0204 (right).

according to the shallow water model. The green curve in Fig. 4 has $b = 1.10$, which is right on the edge. Moreover, the minimum vorticity in the ring is $-0.27 \times 10^{-4}\,\mathrm{s}^{-1}$, which compares favourably with the model value of $-0.21 \times 10^{-4}\,\mathrm{s}^{-1}$ for $b = 1.35$. The model results were for isolated cyclones; they did not capture the change in sign of velocity at $r \approx 4{,}000\,\mathrm{km}$ or the upturn of vorticity beyond 5,000 km, both of which reflect the presence of circumpolar cyclones circling the pole.

The 200 km scale of vorticity and divergence is at least consistent with convection, Severe thunderstorms on Earth have diameters of 30–40 km, which is about five times the pressure scale height[43,44]. Granules, which are the convective elements in the solar photosphere, are about 1,000 km in diameter[45], which is also about five times the scale height of the partially ionized hydrogen gas. The scale height on Jupiter is about 40 km at the water cloud base, so if the ratio of horizontal diameter to scale height were 5, as it is on Earth and the Sun, then convection elements on Jupiter would have diameters of 200 km. This is about the smallest scale we can measure.

The bottom row of Fig. 3 shows no correlation between divergence and vorticity, although both positive and negative values are

Table 1 | Standard deviations of vorticity and divergence for four different sizes of the box used to measure vorticity and divergence

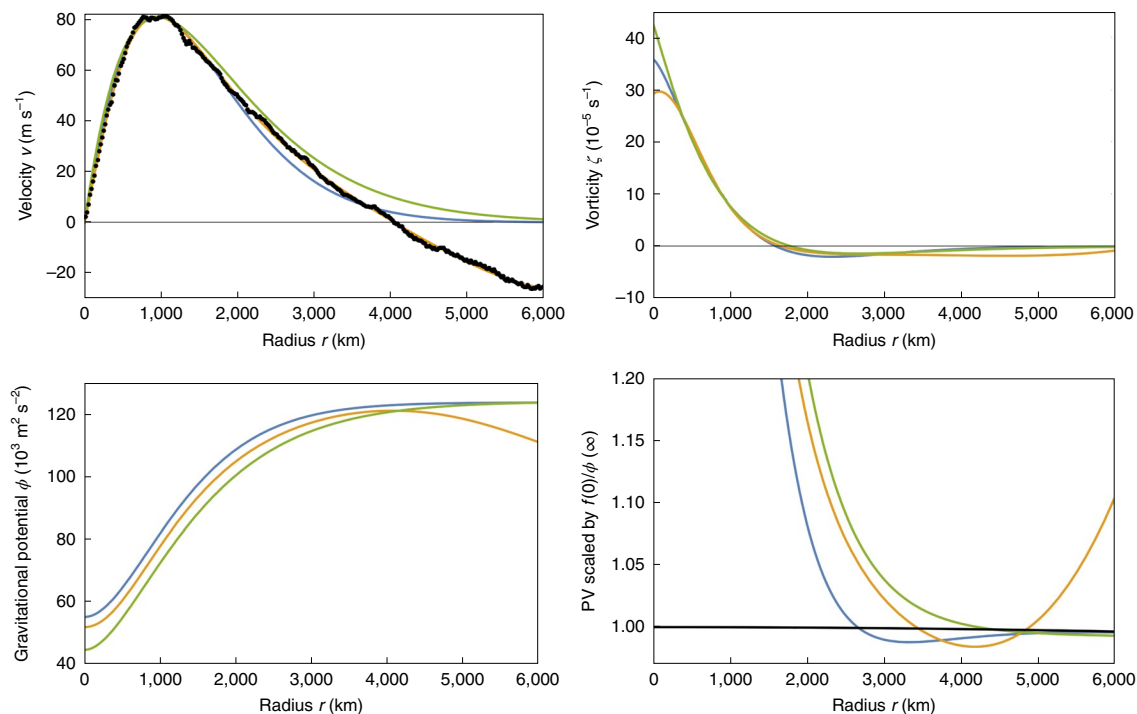| Box size (km x km)	η	Signal (10⁻⁴ s⁻¹)	Noise (10⁻⁴ s⁻¹)
Vorticity			
90 × 90	0.501929	0.754479	0.751573
180 × 180	0.728803	0.623902	0.380587
270 × 270	0.861097	0.556075	0.223338
360 × 360	0.816752	0.469033	0.222166
Divergence			
90 × 90	0.243513	0.435793	0.768104
180 × 180	0.299018	0.264942	0.405655
270 × 270	0.277184	0.1736	0.223076
360 × 360	0.289037	0.100508	0.157633

η is dimensionless.

Fig. 4 | Mean azimuthal velocity and vorticity and mean gravitational potential and potential vorticity. Top left: the fitted curve for velocity (orange) is almost covered by the data points (black). Top right: the peak relative vorticity ζ at the pole is $2.9 \times 10^{-4}\,s^{-1}$, and is almost equal to the polar planetary vorticity f, which is $3.5 \times 10^{-4}\,s^{-1}$. Bottom left: the gravitational potential ϕ is uncertain by an additive constant. Potential vorticity is scaled by $2.843 \times 10^{-9}\,m^{-2}\,s$, which is f at the pole divided by ϕ assuming it is equal to $L_d^2 f^2 = \times 10^3\,m^2\,s^2$, corresponding to $L_d = 1{,}000\,km$. Under this assumption, the scaled PV at the pole is 4.18. The variations in PV are mostly due to variations in ζ and ϕ and less due to variations in f, which is the red line sloping gently down to the right. The other two curves (blue and green) were chosen to bracket the data and were used as initial conditions in a model study[21] that is described in the Discussion. The data points are given in Supplementary Data 3.

present. The implications for convection are uncertain. On the one hand, if a parcel conserves PV around a cycle of updrafts and downdrafts, the material derivative of $\zeta + f$ is proportional to the material derivative of ϕ throughout the cycle. But as ϕ is proportional to h, the material derivative of ϕ is also proportional to minus the divergence $\nabla \cdot \mathbf{v}$. Equivalently, the material derivative of negative (that is, anticyclonic) ζ is proportional to the divergence. As a result, negative vorticity lags the divergence by a quarter cycle and there is no measurable correlation. On the other hand, if a parcel has its vorticity reset to zero at the start of each updraft, then negative vorticity develops on rising trajectories, because they diverge at the top. In this case there is a correlation between divergence and negative vorticity, and that would be a sign of convection.

Our feature-tracking approach yields vorticity and divergence at spatial scales of 200 km and larger. An entirely different approach[20] is to use infrared brightness itself as a dynamical variable, which extends the spatial scale down to wavelengths of ~15 km. The study[20] assumes that negative infrared brightness anomalies, which are related to cloud height, are upward displacements of pressure surfaces and therefore a measure of anticyclonic vorticity. This assumption is verified at scales from 250 to 1,600 km, which are smaller than the large cyclones but large enough that feature tracking is possible. It further assumes that the flow is quasigeostrophic, so the divergence is given by $-1/f$ times the material rate of change of vorticity. This is the surface quasigeostrophic model[46,47], which is used in meteorology and oceanography[48,49]. Applied to Jupiter[20], one observes the signature of convection—a negative correlation between divergence and vorticity at 100 km scales and an upscale energy transfer from scales less than ~200 km to scales greater than ~200 km. These scales are just below the reach of our feature-tracking

method. However, the quasigeostrophic approximation is based on $Ro = \zeta/f \ll 1$, where Ro is the Rossby number. The inequality is not strictly valid for Jupiter's polar cyclones (Fig. 4), and it is even less valid at smaller scales as Ro is predicted to increase with horizontal wavenumber[46].

At mid-latitudes a downscale energy transfer is observed[50], from wavelength scales of 2,000 km to the shortest scale measured, which is about 500 km. That study[50] used Cassini visible light imaging; ours used Juno infrared imaging, and the surface quasigeostrophic model uses infrared brightness. More work is needed to reconcile these three datasets. A parallel study[51] of Jupiter's south polar vortices, focusing on vorticity and stability, represents a step in the right direction.

Methods

A series of 12 images was started every 8 min to cover the same region at the north pole of Jupiter. Ideally the images in a series would fit together like tiles in a mosaic with no overlap and no spaces in between. The spacecraft was approaching Jupiter, and the image resolution changed from 22 km per pixel in the middle of the first series to 14 km per pixel in the middle of the fourth series, 24 min later. The two maps on the left of Fig. 2 were made by measuring cloud displacements between the first and third series, which are 16 min apart, and the two maps on the right were made from the second and fourth series, which are also 16 min apart. Therefore, the left and right maps are separated in time by only 8 min, but use entirely different images.

Supplementary Table 1 contains the archival filenames and our working names for the 48 images that were used in the analysis. The four series are named n01 to n04, each of which recorded roughly the same place on the planet 8 min after the one before. The first step in the processing was to determine the precise location on the planet of each resolution element in each image. This was done with NAIF/SPICE data from the spacecraft and the precise geometric calibration of the JIRAM instrument. The second step was to map the brightness patterns onto a gridded reference plane tangent to the planet at the pole. We used 15 km per pixel for this mapping. These data are provided in Supplementary Data 1.

The third step was to measure cloud displacements in the reference plane using the Tracker3 software from JPL. The software automatically searches for the best correlation of brightness patterns between two images. This was done between images in series n01 and n03 and between images in series n02 and n04. Velocity was the displacement in kilometres divided by the time interval, which was always close to 16 min but depended on which image in each series was used. Correlation was done within a square box in the reference plane. After experimenting, we settled on a 15 × 15 pixel correlation box for the Tracker3 software. Thus, with 15 km per pixel in the reference plane, we were using squares 225 km on a side to define a feature. The resolution of the wind measurement was therefore ±112.5 km. We oversampled it by a factor of 2.5 to obtain wind vectors on a 45 km × 45 km grid. That dataset is Supplementary Data 2. We determined vorticity and divergence at every grid point by integrating around boxes of various sizes using Stokes's theorem and Gauss's law, respectively. Table 1 gives results for boxes 2, 4, 6 and 8 pixels on a side, corresponding to 90, 180, 270 and 360 km on a side, respectively.

The error in the velocity estimate σ_v depended crucially on the granularity of the scene at the scale of the resolution element δ, which on average was about 18 km. Except for areas where there were no features at all, for which there were no estimates, the worst case was a single cloud feature of size $\leq\delta$, for which the variance $\sigma_v^2 = 2\delta^2/\Delta t^2$, where Δt is the 16 min time step and the factor of 2 arises because we are subtracting position in two images. Then $\sigma_v = 2^{1/2}\delta/\Delta t$, about 26.5 m s^{-1}. However, if the velocity measurement is the average of N statistically independent estimates of velocity, the variance is $2\delta^2/\Delta t^2/N$. The best-case scenario is when N is the number of resolution elements in the correlation box of L on a side such that $N = (L/\delta)^2$. Then $\sigma_v = 2^{1/2}\delta/\Delta t/N^{1/2} = 2^{1/2}\delta^2/L/\Delta t$, which is 2.1 m s^{-1} for $L = 225$ km. Thus σ_v is highly uncertain, but in Supplementary Table 2 we show that $\sigma_v = 7.81$ m s^{-1} gives a good fit to the noise column in Table 1.

A quantitative measure of granularity is provided by image entropy H (ref. [52]). We define it for each 15 × 15 correlation box from the histogram of brightness values in the box:

$$H = -\sum p_k \log_2(p_k) \tag{3}$$

The input data were 32 bit numbers, but we only had 225 pixels. We divided the range from the brightest to the darkest pixel into 256 grey levels, and we counted the number of times that each grey level appeared in the image. That number divided by 225 is p_k, the frequency of occurrence of grey level k normalized so that $\sum p_k = 1$. The sum is over the 256 grey levels. If the brightness corresponding to a particular grey level k1 did not occur in the image, then $p_{k1} = 0$. At least 31 of the p_k values must be zero. If all 225 pixels have brightnesses corresponding to grey level k2, then $p_{k2} = 1$ and all the other $p_k = 0$, resulting in $H = 0$. If the brightness levels of all the 225 pixels are different, then $H = \log_2(225) = 7.81$. This is the maximum entropy for this problem. Low entropy is bad for feature tracking, and we experimented to find a value that eliminated the most suspicious data, such as the large pixel-to-pixel variations in the upper left and lower right corners of the divergence maps. We manually verified that the feature-tracking software was failing in those regions. Supplementary Fig. 5 is a histogram of entropy values, and Supplementary Figs 6 and 7 compare the vorticity and divergence maps with the low-entropy data present and with them masked out.

The data in Fig. 4 consisted of ~26,000 measured velocity vectors on the 45 km × 45 km grid of $r < 6,010$ km. Taking the azimuthal component $\bar{v}(r)$ of each vector, and knowing its r, we performed two separate least squares fits, one for a_n and the other for b_n in equation (2) to get analytic expressions for $\bar{v}(r)$ and $\partial\bar{\phi}(r)/\partial r$, respectively.

$$\bar{v} = \sum_1^4 a_n r^n + \frac{a_5 r}{(r^2 + r_0^2)}, \quad \frac{\partial\bar{\phi}}{\partial r} = -\frac{\bar{v}^2}{r} - 2\Omega\bar{v} = \sum_1^4 b_n r^n + \frac{b_5 r}{(r^2 + r_0^2)}. \tag{4}$$

This choice of functions had no physical significance. The functions were chosen simply to fit the data and provide analytic expressions for integration and differentiation. For a good fit, the parameter r_0 must be close to the radius of the velocity maximum. From visual inspections, it was chosen to be 1,060 km for $\partial\bar{\phi}/\partial r$ and 1,200 km for $\bar{v}$. We analytically integrated the expression for cyclostrophic balance in equation (2) to get $\bar{\phi}(r)$ in Fig. 4, and we analytically differentiated the expression $(1/r)\partial(r\bar{v})/\partial r = \bar{\zeta}$ to obtain vorticity. The measured azimuthal velocities are available in Supplementary Data 3.

Data availability

JIRAM data are available online at the Planetary Data System (PDS) at https://pds-atmospheres.nmsu.edu/data_and_services/atmospheres_data/JUNO/jiram. The filenames of the images are listed in Supplementary Table 1. Calibrated, geometrically controlled radiance data mapped onto an orthographic projection centred on the north pole and velocity vectors derived from the radiance data are available in Supplementary Data 1–2.

References

1. Orton, G. S. et al. The first close-up images of Jupiter's polar regions: results from the Juno mission JunoCam instrument. *Geophys. Res. Lett.* **44**, 4599–4606 (2017).
2. Adriani, A. et al. Clusters of cyclones encircling Jupiter's poles. *Nature* **555**, 216–219 (2018).
3. Tabataba-Vakili, F. et al. Long-term tracking of circumpolar cyclones on Jupiter from polar observations with JunoCam. *Icarus* **335**, 113405 (2020).
4. Adriani, A. et al. Two-year observations of the Jupiter polar regions by JIRAM on board Juno. *J. Geophys. Res.* https://doi.org/10.1029/2019JE006098 (2020).
5. Mura, A., Adriani, A. & Bracco, A. Oscillations and stability of the Jupiter polar cyclones. *Geophys. Res. Lett.* **48**, e2021GL094235. https://doi.org/10.1029/2021GL0942235 (2021).
6. Grassi, D. et al. First estimate of wind fields in the Jupiter polar regions from JIRAM-Juno images. *J. Geophys. Res. Planets* **123**, 1511–1524 (2018).
7. Orton, G. S. & Yanamandra-Fisher, P. A. Saturn's temperature field from high-resolution middle-infrared imaging. *Science* **307**, 696–698 (2005).
8. Dyudina, U. A. et al. Dynamics of Saturn's south polar vortex. *Science* **319**, 1801 (2008).
9. Dyudina, U. A. et al. Saturn's south polar vortex compared to other large vortices in the Solar System. *Icarus* **202**, 240–248 (2009).
10. Sommeria, J., Meyers, S. & Swinney, H. Laboratory model of a planetary eastward jet. *Nature* **337**, 58–61 (1989).
11. Allison, M., Godfrey, D. & Beebe, R. A wave-dynamic interpretation of Saturn's polar hexagon. *Science* **247**, 1061–1063 (1990).
12. Aguiar, A. C. B., Read, P. L., Wordsworth, R. D., Salter, T. & Yamazaki, Y. H. A laboratory model of Saturn's North Polar Hexagon. *Icarus* **206**, 755–763 (2010).
13. Sanchez-Lavega, A. et al. The long-term steady motion of Saturn's hexagon and the stability of its enclosed jet stream under seasonal changes. *Geophys. Res. Lett.* **41**, 1425–1431 (2014).
14. Morales-Juberias, R., Sayanagi, K. M., Simon, A. A., Fletcher, L. N. & Cosentino, R. G. Meandering shallow atmospheric jet as a model of Saturn's north-polar hexagon. *Astrophys. J.* **806**, 1–6 (2015).
15. Scott, R. K. Polar accumulation of cyclonic vorticity. *Geophys. Astrophys. Fluid Dynam.* **105**, 409–420 (2011).
16. O'Neill, M. E., Emanuel, K. A. & Flierl, G. R. Polar vortex formation in giant-planet atmospheres dues to moist convection. *Nat. Geosci.* **8**, 523–526 (2015).
17. O'Neill, M. E., Emanuel, K. A. & Flierl, G. R. Weak jets and strong cyclones: shallow-water modeling of giant planet polar caps. *J. Atmos. Sci.* **73**, 1841–1855 (2016).
18. Brueshaber, S. R., Sayanagi, K. M. & Dowling, T. E. Dynamical regimes of giant planet polar vortices. *Icarus* **323**, 46–61 (2019).
19. Siegelman, L., Young, W. R. & Ingersoll, A. P. Polar vortex crystals: emergence and structure. *Proc. Natl Acad. Sci. USA* **119**, e2120486119 (2022).
20. Siegelman, L. et al. Moist convection drives an upscale energy transfer at Jovian high latitudes. *Nat. Phys.* **18**, 357–361 (2022).
21. Li, C., Ingersoll, A. P., Klipfel, A. P. & Brettle, H. Modeling the stability of polygonal patterns of vortices at the poles of Jupiter as revealed by the Juno spacecraft. *Proc. Natl Acad. Sci. USA* **117**, 24082–24087 (2020).
22. Thomson, S. I. & McIntyre, M. E. Jupiter's unearthly jets: a new turbulent model exhibiting statistical steadiness without large-scale dissipation. *J. Atmos. Sci.* **73**, 1119–1141 (2016).
23. Rubio, A. M., Julien, K., Knobloch, E. & Weiss, J. B. Upscale energy transfer in three-dimensional rapidly rotating turbulent convection. *Phys. Rev. Lett.* **112**, 144501 (2014).
24. Novi, L., von Hardenberg, J., Hughes, D. W., Provenzale, A. & Spiegel, E. A. Rapidly rotating Rayleigh-Benard convection with a tilted axis. *Phys. Rev. E* **99**, 053116 (2019).
25. Yadav, R. K., Heimpel, M. & Bloxham, J. Deep convection-driven vortex formation on Jupiter and Saturn. *Sci. Adv.* **6**, eabb9298 (2020).
26. Kapyla, P. J., Mantere, M. J. & Hackman, T. Starspots due to large-scale vortices in rotating turbulent convection. *Astrophys.* **742**, 34 (2011).
27. Heimpel, M., Gastine, T. & Wicht, J. Simulation of deep-seated zonal jets and shallow vortices in gas giant atmospheres. *Nat. Geosci.* **9**, 19–23 (2016).
28. Cai, T., Chan, K. L. & Mayr, H. G. Deep closely packed long-lived cyclones on Jupiter's poles. *Planet. Sci. J.* **2**, 81 (2021).
29. Ingersoll, A. & Cuzzi, J. Dynamics of Jupiter's cloud bands. *J. Atmos. Sci.* **26**, 981–985 (1969).
30. Limaye, S. Jupiter: new estimates of the mean zonal flow at the cloud level. *Icarus* **65**, 335–352 (1986).
31. Li, L. M. et al. Life cycles of spots on Jupiter from Cassini images. *Icarus* **172**, 9–23 (2004).
32. Garcia-Melendo, E., Perez-Hoyos, S., Sanchez-Lavega, A. & Hueso, R. Saturn's zonal wind profile in 2004–2009 from Cassini ISS images and its long-term variability. *Icarus* **215**, 62–74 (2011).
33. Dowling, T. A relationship between potential vorticity and zonal wind on Jupiter. *J. Atmos. Sci.* **50**, 14–22 (1993).

34. Achterberg, R. & Ingersoll, A. A normal-mode approach to Jovian atmospheric dynamics. *J. Atmos. Sci.* **46**, 2448–2462 (1989).
35. Wong, M. H., de Pater, I., Asay-Davis, X., Marcus, P. S. & Go, C. Y. Vertical structure of Jupiter's Oval BA before and after it reddened: what changed? *Icarus* **215**, 211–225 (2011).
36. Hammel, H. et al. HST Imaging of atmospheric phenomena created by the impact of Comet Shoemaker-Levy-9. *Science* **267**, 1288–1296 (1995).
37. Rhines, P. Waves and turbulence on a beta-plane. *J. Fluid Mech.* **69**, 417–443 (1975).
38. Theiss, J. Equatorward energy cascade, critical latitude, and the predominance of cyclonic vortices in geostrophic turbulence. *J. Phys. Oceanogr.* **34**, 1663–1678 (2004).
39. Scott, R. K. & Polvani, L. M. Forced-dissipative shallow-water turbulence on the sphere and the atmospheric circulation of the giant planets. *J. Atmos. Sci.* **64**, 3158–3176 (2007).
40. Mied, R. & Lindemann, G. Propagation and evolution of cyclonic Gulf-Stream rings. *J. Phys. Oceanogr.* **9**, 1183–1206 (1979).
41. Chassignet, E. & Cushman-Roisin, B. On the influence of a lower layer on the propagation of nonlinear oceanic eddies. *J. Phys. Oceanogr.* **21**, 939–957 (1991).
42. Adriani, A. et al. JIRAM, the Jovian Infrared Auroral Mapper. *Space Sci. Rev.* **213**, 393–446 (2017).
43. Garcia-Ortega, E., Lopez, L. & Sanchez, J. L. Diagnosis and sensitivity study of two severe storm events in the Southeastern Andes. *Atmos. Res.* **93**, 161–178 (2009).
44. Marion, G. R. & Trapp, R. J. The dynamical coupling of convective updrafts, downdrafts, and cold pools in simulated supercell thunderstorms. *J. Geophys. Res. Atmos.* **124**, 664–683 (2019).
45. Solov'ev, A. A., Parfinenko, L. D., Efremov, V. I., Kirichek, E. A. & Korolkova, O. A. Structure of photosphere under high resolution: granules, faculae, micropores, intergranular lanes. *Astrophys. Space Sci.* **364**, 222 (2019).
46. Juckes, M. Quasi-geostrophic dynamics of the tropopause. *J. Atmos. Sci.* **51**, 2756–2768 (1994).
47. Held, I. M., Pierrehumbert, R. T., Garner, S. T. & Swanson, A. Surface quasi-geostrophic dynamics. *J. Fluid Mech.* **282**, 1–20 (1995).
48. Lapeyre, G. & Klein, P. Dynamics of the upper oceanic layers in terms of surface quasigeostrophy theory. *J. Phys. Oceanogr.* **36**, 165–176 (2006).
49. Lapeyre, G. Surface quasi-geostrophy. *Fluids* **2**, 7–28 (2017).
50. Young, R. M. B. & Read, P. L. Forward and inverse kinetic energy cascades in Jupiter's turbulent weather layer. *Nat. Phys.* **13**, 1135–1140 (2017).
51. Gonzalez, R. C. & Woods, R. E. *Digital Image Processing* (Pearson, 2016).
52. Scarica, P. et al. Stability of the Juoter southern polar vortices inspected through vorticity using Juno/JIRAM data. *J. Geophys. Res., Planets*, https://doi.org/10.1029/2021JE007159 (2021).

Acknowledgements

Author contributions

A.P.I. led the research and wrote the document. S.P.E. conducted the data analysis and prepared the figures. F.T. prepared the geometric tables that were used in the analysis. A.A., A.M., D.G., C.P. and G.S. oversaw the successful functioning of the JIRAM instrument and provided expertise on using it for image processing. C.L., L.S., P.K. and W.R.Y. provided expertise on vortices.

Competing interests

The authors declare no competing interests.

Additional information